Mineralium Deposita (2020) 55:293–308
https://doi.org/10.1007/s00126-019-00882-8

ARTICLE

Geochronological and sulfur isotopic evidence for the genesis of the post-magmatic, deeply sourced, and anomalously gold-rich Daliuhang orogenic deposit, Jiaodong, China

Kai Feng[1,2] · Hong-Rui Fan[1,2,3] · David I. Groves[4,5] · Kui-Feng Yang[1,2,3] · Fang-Fang Hu[1,2,3] · Xuan Liu[1,6] · Ya-Chun Cai[1]

Received: 8 January 2019 / Accepted: 25 March 2019 / Published online: 15 April 2019

Abstract

The Daliuhang gold deposit (> 20 t gold) is located in the central Penglai-Qixia belt of the giant Jiaodong gold province, eastern China. The ore-hosting Guojialing granodiorite and pegmatite were formed at 129.0 ± 0.6 Ma and 126.2 ± 0.6 Ma, respectively. Syn-ore monazite, with a U–Pb age of 120.5 ± 1.7 Ma, represents the timing of gold mineralization. Given at least 5 m.y. between magmatism and mineralization, a genetic relationship to magmatic-hydrothermal activity is negated. Noble gas isotopes of pyrite have crust-mantle-mixed $^{3}He/^{4}He$ (1.13 to 1.50 Ra) and air-like $^{40}Ar/^{36}Ar$ (327–574). Together with the broadly positive correlation between ^{3}He and ^{36}Ar, it is inferred that the initial ore-forming fluids were deeply sourced from the sedimentary wedge overlying the subducted plate and overlying mantle during early Cretaceous paleo-Pacific plate subduction. The pre-ore and post-ore pyrites have low $\delta^{34}S$ values (3.7–5.6‰ and 5.3–6.4‰, respectively), whereas ore-related pyrites have higher $\delta^{34}S$ values, especially in As–Au-rich domains (7.8–8.3‰). These positive $\delta^{34}S$ values also suggest that the initial ore fluid and some of the sulfur component were derived via subduction-related devolatilization. The elevated $\delta^{34}S$ values of the ore-related pyrite are partly ascribed to mass fractionation and partly to a contribution from sulfur leached from crustal host rocks. This interpretation is also supported by neodymium isotope ratios of monazite (ε_{Nd} (~ 120 Ma) = − 13.7 to − 11.6), which correlate well with the ore-hosting Guojialing granodiorite. This study highlights the combined roles of deeply derived fluids and intense interaction with upper crustal rocks in the formation of Jiaodong gold deposits.

Keywords Monazite U–Pb geochronology · In situ sulfur isotopes · He–Ar isotopes · Deeply sourced gold fluid · Orogenic gold deposit · Jiaodong

Introduction

The Jiaodong Peninsula is the largest and most productive gold province in China, with more than 5000 t of gold resources (Song 2015; Yang et al. 2016; Fan et al. 2016; Liu et al. 2017; Yang et al. 2018). In this region, abundant disseminated-style and auriferous quartz vein–style deposits are hosted in Mesozoic granitoids. Previous studies show that the deposits were formed in the Mesozoic (120 ± 10 Ma), generally contemporaneous with basic to felsic magmatism in the

Editorial handling: B. Lehmann

Electronic supplementary material The online version of this article (https://doi.org/10.1007/s00126-019-00882-8) contains supplementary material, which is available to authorized users.

✉ Hong-Rui Fan
fanhr@mail.iggcas.ac.cn

[1] Key Laboratory of Mineral Resources, Institute of Geology and Geophysics, Chinese Academy of Sciences, Beijing 100029, China

[2] College of Earth and Planetary Science, University of Chinese Academy of Sciences, Beijing 100049, China

[3] Institutions of Earth Science, Chinese Academy of Sciences, Beijing 100029, China

[4] State Key Laboratory of Geological Processes and Mineral Resources, China University of Geosciences, Beijing 100083, China

[5] Centre for Exploration Targeting, University of Western Australia, Nedlands 6009, Australia

[6] GeoRessources Lab, Université de Lorraine, CNRS, CREGU, 54500 Vandœuvre-lès-Nancy, France

region (Yang et al. 2003, 2004; Fan et al. 2007; Hou et al. 2007a; Cai et al. 2013; Ma et al. 2017; Li et al. 2019). However, whether or not magmatism directly provided fluid, metal, or energy for the gold mineralization is still not well understood.

To better understand this issue, the Daliuhang deposit, which is a representative deposit in this region, was chosen for study. Located in central Jiaodong and hosted in early Cretaceous granodiorite, the Daliuhang deposit is a typical auriferous quartz vein–style gold deposit. This deposit has high-grade gold ores (20 g/t on average), and locally contains visible gold (Zhou and Zhang 1997; Chang et al. 2013; Yang et al. 2018). In addition, there are abundant mafic and felsic dykes that are broadly coeval with gold mineralization in the mining district. Thus, the Daliuhang deposit represents an excellent example to investigate the possible genetic relationship between gold mineralization and magmatism.

In this study, the U–Pb age of hydrothermal monazite in the ores was obtained to delineate the precise timing of gold mineralization for the Daliuhang deposit. In addition, the U–Pb ages of zircon from ore-hosting granite, a pegmatite dyke, and two mafic dykes were obtained, collectively, to determine the timing of relevant basic and felsic magmatic events. In situ sulfur isotopic analyses on gold-hosted pyrite, in situ Nd isotopic analyses on hydrothermal monazite, and He–Ar isotopic analyses on primary ore-forming fluids entrapped in pyrite were conducted in order to place constraints on the sources and temporal evolution of the ore-forming fluids, and also on the possible sources of sulfur and ore metals. The integrated results allow a better understanding of the genesis of the Daliuhang deposit.

Regional geology

The Jiaodong Peninsula is located on the southeastern edge of the North China Craton (NCC). It comprises the Sulu ultrahigh pressure (UHP) orogen in the southeast and the Jiaobei Terrane in the northwest (Fig. 1). Almost all gold deposits are distributed in the Jiaobei Terrane, which mainly comprises Precambrian basement rocks and Mesozoic magmatic intrusions and volcanic-sedimentary sequences (Zhai and Santosh 2013; Wen et al. 2015). The Precambrian basement rocks include Archean metamorphic volcanic-sedimentary rocks and tonalite-trondhjemite-granodiorite (TTG) gneisses (the Jiaodong Group), Paleoproterozoic meta-volcanic and meta-sedimentary rocks (the Jingshan and Fenzishan Groups), and Neoproterozoic meta-sedimentary rocks of the Penglai Group

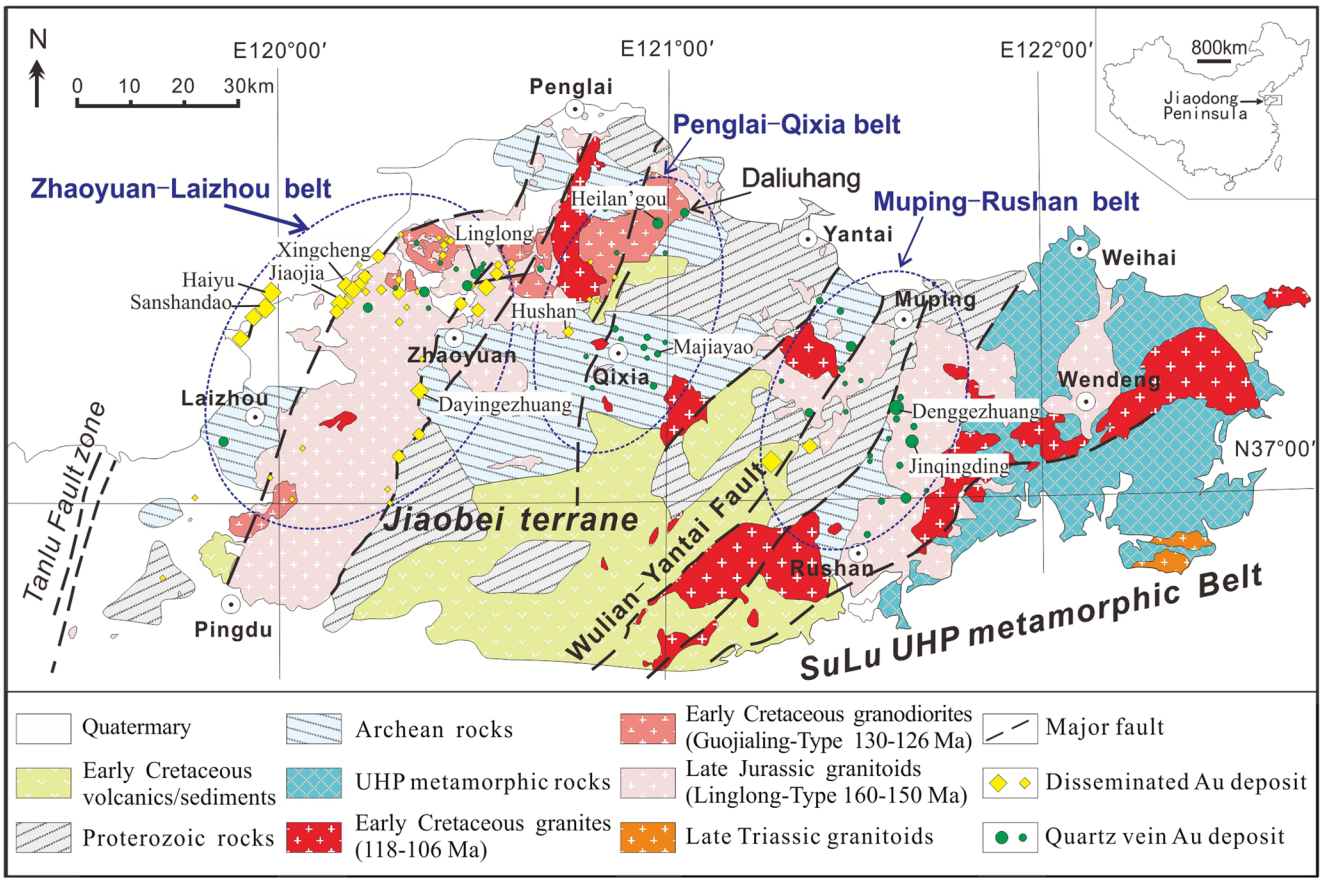

Fig. 1 Geological map of the Jiaodong gold province, showing the major gold deposits and lithological units. Modified after Wen et al. (2015)

(Zhou and Lü 2000; Zhai and Santosh 2013; Zou et al. 2017). Mesozoic igneous intrusions form three groups: (1) late Jurassic (160–150 Ma) plutons represented by the Linglong biotite granite and Luanjiahe monzogranite, (2) early Cretaceous (130–126 Ma) plutons represented by the Guojialing granodiorite, and (3) early Cretaceous (118–110 Ma) plutons represented by the Aishan porphyritic syenogranite and monzogranite (Miao et al. 1997; Hou et al. 2007b; Yang et al. 2012; Jiang et al. 2016; Li et al. 2018, 2019). Mesozoic volcanic-sedimentary sequences that occur in the south-central part of the Jiaobei Terrane (Liu et al. 2009; Xie et al. 2012; Wang et al. 2016) include a basal lacustrine sedimentary sequence (the Laiyang Group, ~ 130 Ma), overlain by intermediate to basic volcanic rocks (the Qingshan Group, ~ 124–98 Ma) and an upper lacustrine sedimentary sequence (the Wangshi Group, ~ 80 Ma).

The Jiaodong gold province is divided, from west to east, into the Zhaoyuan-Laizhou, Penglai-Qixia, and Muping-Rushan belts (Fig. 1). Most gold deposits are hosted in the Linglong and Guojialing granitoids or their contacts with the basement metamorphic rocks (Fig. 1). The distribution of gold deposits is controlled by a set of NE- and NNE-trending crustal-scale fault zones, including the Sanshandao, Jiaojia, Zhaoping, Qixia, and Muping fault zones. Gold deposits of this district have been traditionally classified as disseminated style and auriferous quartz vein style (Zhou and Lü 2000; Fan et al. 2007; Goldfarb and Santosh 2014; Wen et al. 2015). The disseminated-style mineralization consists of disseminated and stockwork ores and is located in regional faults, which are enveloped by broad alteration halos. The auriferous quartz vein–style mineralization is characterized by abundant auriferous quartz veins hosted in the subsidiary second- or third-order faults. Most of the large disseminated-style deposits are located in the Zhaoyuan-Laizhou gold belt, which hosts almost 90% of the gold reserves of the Jiaodong Peninsula (Song 2015; Yang et al. 2016; Fan et al. 2016). In contrast, the Penglai-Qixia belt is characterized by a number of medium- to large-sized, quartz vein–style gold deposits, with the exception being the recently discovered disseminated-style Hushan deposit (Feng et al. 2018; Yang et al. 2018).

Ore deposit geology

The Daliuhang gold deposit, with a proven reserve of > 20 t gold, is situated in the northern segment of the Penglai-Qixia gold belt. Granitoids are widely distributed in the mining district, and include the late Jurassic Linglong gneissic biotite granite and early Cretaceous Guojialing granodiorite (Fig. 2a). Precambrian metamorphic rocks occur along the contacts between the abovementioned different granitoids in places. Late-magmatic pegmatite and aplite dykes are well developed within the Guojialing granodiorite (Fig. 3a–c). Ultramafic to intermediate dykes, including lamprophyre, dolerite, diorite, and porphyrite, are also abundant (Figs. 3c, d and 7a, b). Some mafic dykes are altered around mineralized quartz veins at Daliuhang (Fig. 7a), whereas others are adjacent to auriferous quartz veins (Fig. 7b), without obvious wall rock alteration, in the adjacent Heilan'gou deposit (Fig. 1).

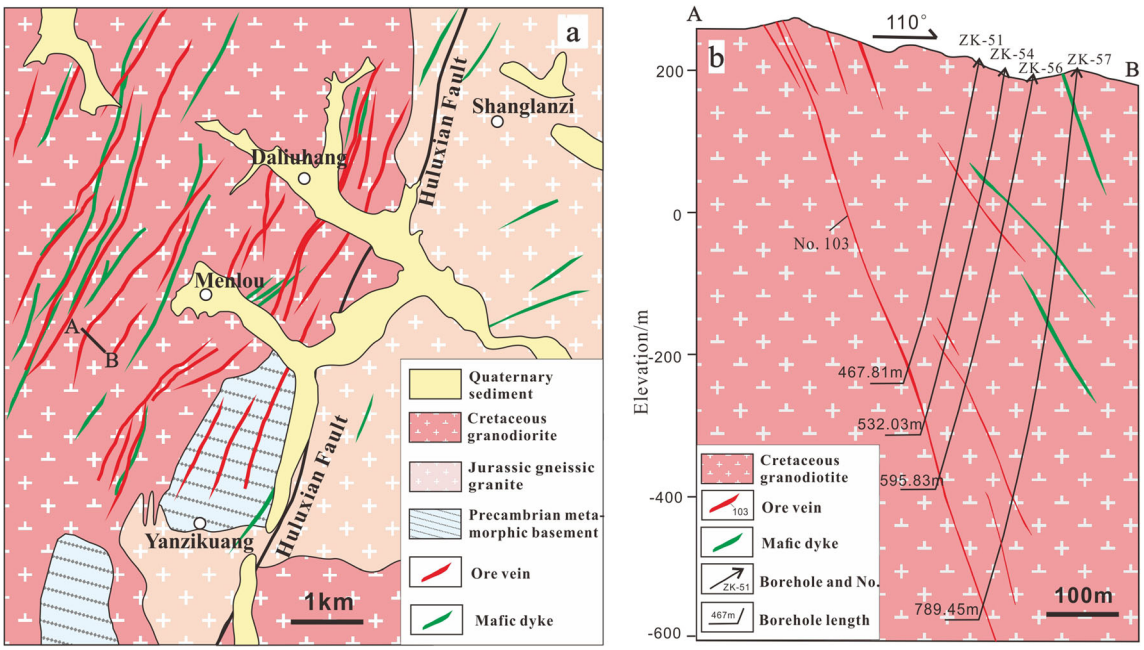

Fig. 2 **a** Geological map of the Daliuhang deposit. **b** Cross-section (A–B) of the orebody no. 103 vein

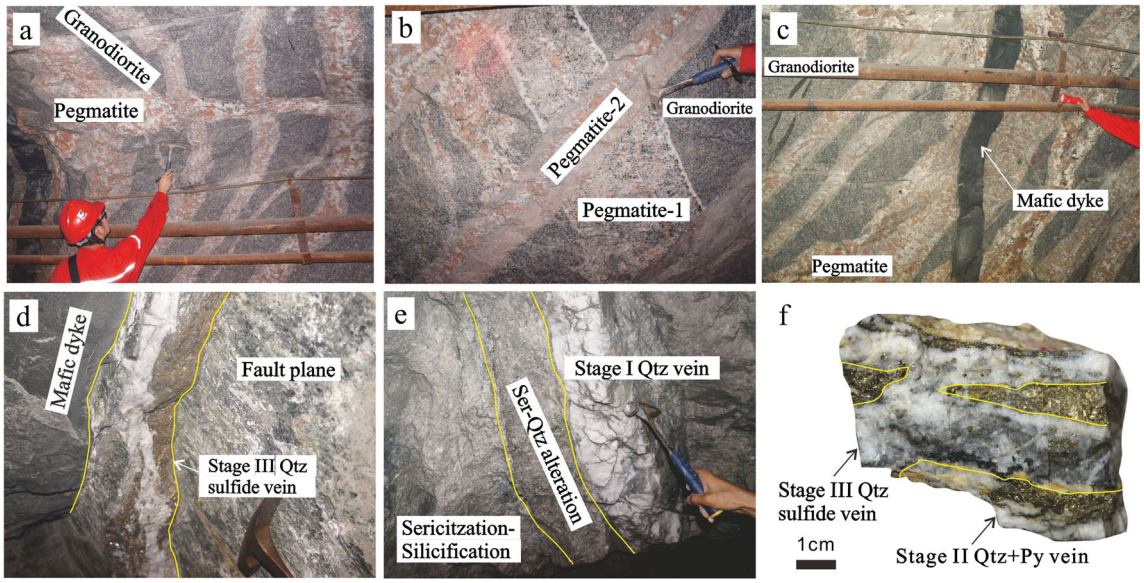

Fig. 3 Photographs of major wall rocks and various mineralized veins in the Daliuhang gold deposit. **a** Multiple pegmatite dykes intrude into Guojialing granodiorite. **b** The earlier pegmatite-1 is cross-cut by later pegmatite-2. **c** Guojialing granodiorite and pegmatite are cross-cut by mafic dyke. **d** Mafic dyke and quartz-sphalerite-galena-pyrite vein (stage III) orebody along fault zones. **e** Quartz vein (stage I) and its adjacent sericite-quartz alteration, sericitization, and silicification. **f** Representative specimens of quartz-pyrite veins (stage II) which are crosscut and overprinted by quartz-galena-pyrite vein (stage III). Py, pyrite; Qtz, quartz; Ser, sericite

The ore bodies are mainly hosted in the Guojialing porphyritic granodiorite, although minor occurrences are hosted within the nearby Precambrian metamorphic rocks close to the surface (Fig. 2a). The mineralization occurs predominantly in the form of massive auriferous quartz veins. Lesser amounts of pyrite-sericite-quartz altered granitic cataclasite occur adjacent to the main lodes. The auriferous quartz veins are controlled by a series of NE- and NNE-trending subsidiary faults in the footwall of the main NNE-trending Huluxian Fault (Fig. 2a). These faults consistently strike 020°–050° and dip 40°–85° SE, with lengths of hundreds to thousands of meters but widths less than a few meters. Most are filled by quartz veins, sericite-quartz-altered cataclasites, and intermediate to mafic dykes.

The no. 103 vein is the most important and representative orebody in this district, with a length of 2.5 km and a width of approximately 0.2 to 2 m. It generally strikes 020°–045°, dips 50°–80° SE, and extends from the surface to below the – 600-m level (Fig. 2b). The gold grade varies from 1.06 to 160.02 g/t, averaging 20.09 g/t (Zhang et al. 2006). The alteration halos, from proximal to distal zones of the veins, include an intense sericite-quartz alteration zone, followed by sericitization, silicification, and K-feldspar alteration zones (Fig. 3e).

Four stages of mineralization in the ore-bearing lodes have been recognized based on cross-cutting relationships between veins and mineral textures within them (Fig. 3d–f). Stage I is characterized by coarse-grained milky quartz with sparsely disseminated fine-grained pyrite (Py1) that contains no gold mineralization. Stage II is represented by quartz-pyrite veins. Pyrite in this stage (Py2) is euhedral to subhedral and appears to be compositionally homogeneous in backscattered electron (BSE) images. Some visible gold grains occur either along the grain boundaries or within fractures of Py2 (Fig. 4a). A few monazite grains were also identified as inclusions in Py2 grains or adjacent to their margins, showing a close spatial association with pyrite (Fig. 5a, b). The anhedral monazite grains have variable diameters (5–100 μm) and are compositionally homogeneous under BSE images. Stage III veins contain coarse-grained quartz and pyrite, with subordinate galena, sphalerite, and chalcopyrite (Fig. 4b, c). Locally, stage III minerals are superimposed on Py2, forming an irregular, dark inner core (marked as Py2-altered) with fine-grained galena overgrown by a bright outer rim (Py3) in BSE images (Fig. 4b), with the rim interpreted to be enriched in arsenic and hence termed “arsenian pyrite” (Feng et al. 2018; Li et al. 2019 and unpublished data from this study). Irregular electrum grains occur along grain boundaries of Py3 where they display a close paragenetic association with galena (Fig. 4d). Stage IV is represented by milky carbonate-quartz veins with minor pyrite (Py4). Stages II and III represent the main gold mineralization episodes.

Sampling and analytical methods

Zircon U–Pb dating

Zircon crystals for U–Pb dating were separated from the ore-hosting Guojialing porphyritic granodiorite (sample 14DLH-01), a pegmatite dyke (sample 14DLH-34), a pre-ore altered

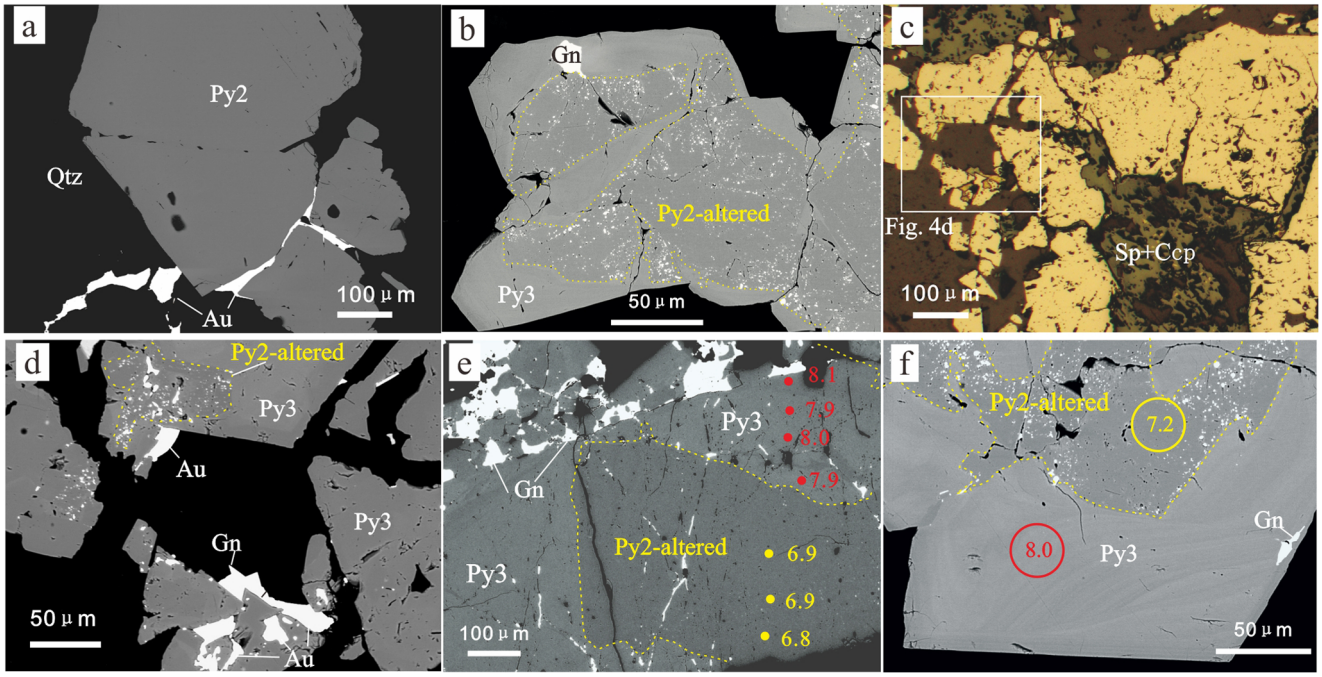

Fig. 4 Backscattered electron (BSE) images (**a**, **b** and **d**–**f**) and reflected light photomicrographs (**c**) showing occurrences of visible gold and textural features of pyrite from main mineralizing stages II and III. **a** Coarse-grained Py2 from quartz-pyrite veins (stage II) is homogeneous in composition and visible gold grains occur in fractures or near the grain boundary. **b** Irregular Py2-altered with porous texture is overgrown by zoned and brighter Py3 from quartz polymetallic sulfide veins (stage III); note that fine-grained and relatively larger galena inclusion are in Py2-altered (core) and Py3 (rim), respectively. **c** Pyrite intergrowth with sphalerite with chalcopyrite exsolution texture in stage III. **d** Detail of image in panel **c**, visible gold grains intergrown with galena along grain boundaries of the Py3. **e** Py2-altered (core) and Py3 (rim) are both infilled by galena. **f** Oscillatory-zoned Py3 that has overgrown the porous Py2-altered. Representative sulfur isotope results are shown in panels **e** (via SIMS) and **f** (via LA-MC-ICPMS). Ccp, chalcopyrite; Gn, galena; Py, pyrite; Qtz, quartz; Sp, sphalerite

mafic dyke (sample 14DLH-14) in the Daliuhang deposit, and a syn-ore mafic dyke (sample 14HLG-06) from the nearby Heilan'gou deposit. The analyses were conducted using an Agilent 7500a ICP-MS equipped with a GeoLas 2005 laser ablation system, at the State Key Laboratory of Geological Processes and Mineral Resources (GPMR), China University of Geosciences (Wuhan). Analyses were performed with a beam diameter of 32 μm and a repetition rate of 6 Hz. Zircon 91500 and GJ-1 were used as the external and monitor standards, respectively. The obtained weighted mean $^{206}Pb/^{238}U$ age for GJ-1 is 602.8 ± 2.3 Ma (MSWD = 0.74, $N = 20$), which is consistent with the reported reference values (599.6 ± 2.9 Ma, Liu et al. 2010), thus ensuring the reliability of the U–Pb data. More detailed analytical conditions and procedures are described by Liu et al. (2010). Data reduction and calibration were performed using ICPMSDataCal (Liu et al. 2010). Uncertainties in ages are quoted at the 95% confidence level.

Monazite U–Pb dating and Nd isotopic analyses

Uranium–Pb dating and Sm–Nd isotopic analyses of monazite, from the gold-bearing quartz-pyrite veins (stage II), were conducted in polished thin sections at the Institute of Geology and Geophysics, Chinese Academy of Sciences (IGGCAS). Before analysis, the target grains were carefully observed under a scanning electron microscope (SEM). Backscattered electron images were used as guidance for spot selection.

Monazite U–Pb dating was conducted by an Agilent 7500a Q-ICP-MS equipped with a COMPex PRO 193-nm excimer laser ablation system. The analytical methods and operating procedures follow the protocols described in Liu et al. (2012). The laser was set at 6-Hz repetition rate and 10 J/cm^2 energy density with 24-μm spot size. Each spot analysis consists of approximately 20-s background acquisition and 45-s sample data acquisition. Monazite 44069 was used as the matrix-matched external standard to correct the U/Pb fractionation and the instrumental mass discrimination (Aleinikoff et al. 2006). Monazite M-1 was measured as monitor standard to evaluate the reliability of results. Six spots yield a weighted mean $^{206}Pb/^{238}U$ age of 524.4 ± 3.9 Ma, which is in good agreement with the reported reference values ($^{206}Pb/^{238}U$ ages, 524.8 ± 3.7 Ma, Liu et al. 2012), and ensure the reliability of the U–Pb data. All data reduction was carried out using the GLITTER 4.0 program (Griffin et al. 2008).

In situ Sm–Nd isotopic compositions of monazite were measured by a Thermo-Finnigan Neptune MC-ICP-MS, equipped with a GeoLas193nm ArF excimer laser ablation system. Analyses were performed with a beam diameter of 16 μm and a repetition rate of 3 Hz. The detailed analytical

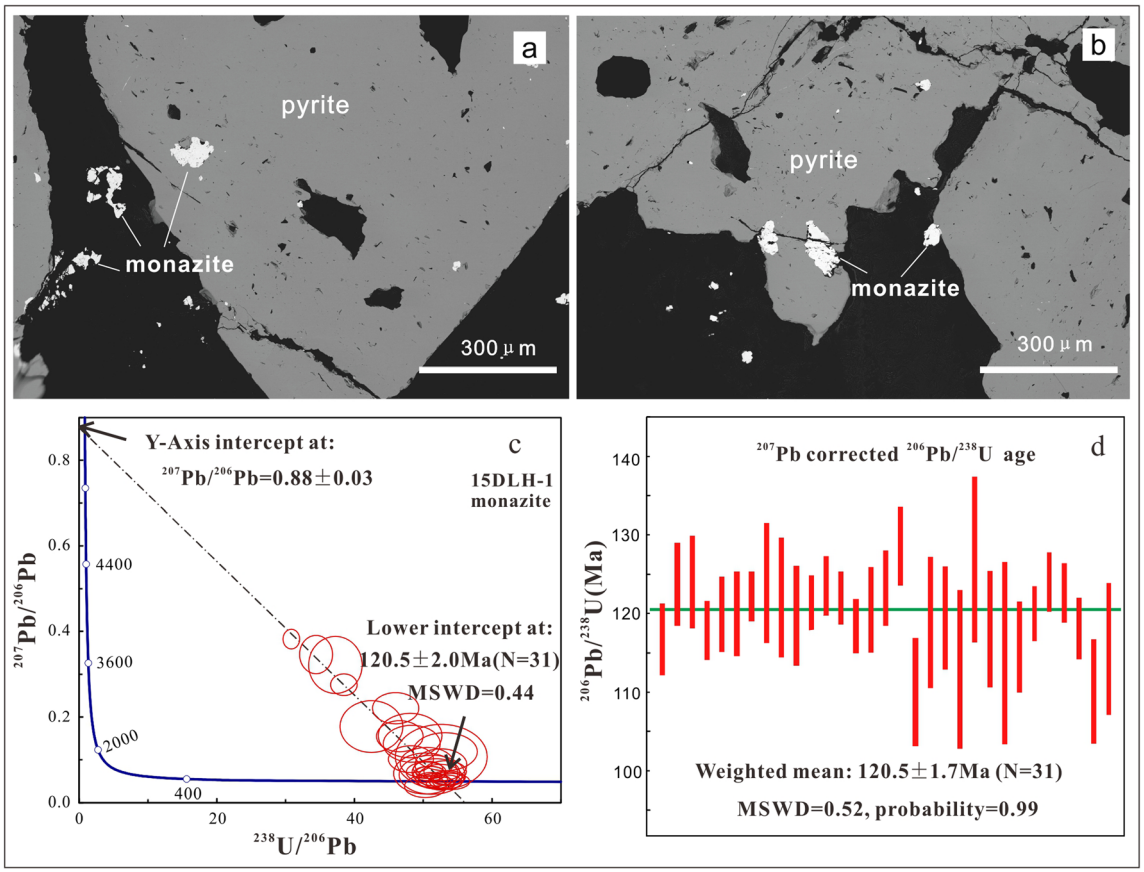

Fig. 5 **a**, **b** Representative monazite crystals, coexisting with pyrite. **c** The U–Pb Tera–Wasserburg Concordia diagram for monazite. **d** The ^{207}Pb-corrected $^{206}Pb/^{238}U$ weighted mean age for monazite

protocol and data calibration are provided in Yang et al. (2008) and Liu et al. (2012). For Nd isotope mass bias correction, $^{146}Nd/^{144}Nd$ was normalized to 0.7219 for the calculation of the mass bias factor. The isobaric interference of ^{144}Sm on ^{144}Nd was calculated using a subtraction equation proposed by Yang et al. (2008), and the mass bias factor for Sm was obtained by using the interference-free $^{147}Sm/^{149}Sm$ (for detailed descriptions, please refer to Liu et al. 2012). During the process of analysis, the fractionation between ^{144}Sm and ^{144}Nd was corrected by calibrating against an external monazite standard Namaqua-1. In addition, monazite Jefferson and 44069 were selected as monitor standards to evaluate the reliability of analyses. The obtained average $^{143}Nd/^{144}Nd$ ratios of Jefferson (0.513059 ± 27, $N = 6$) and 44069 (0.512161 ± 21, $N = 9$) are consistent with the reference values by LA-MC-ICPMS (Jefferson: $^{143}Nd/^{144}Nd = 0.513057 \pm 93$; 44069: $^{143}Nd/^{144}Nd = 0.512175 \pm 40$, Liu et al. 2012).

He–Ar isotopic analyses

The noble-gas isotope analyses of fluid inclusions in pyrite from auriferous quartz veins were conducted using a Noblesse mass spectrometer at IGGCAS. All pyrite crystals were handpicked from the crushed ore under the microscope. After washing and drying, each sample (about 1 g) was loaded into the crusher chamber and then baked under vacuum for three days to avoid any adsorbed atmospheric gases. One-step or multi-step crushing extractions were carried out on all samples in order to analyze the noble gases trapped in fluid inclusions at 2000-psi pressure. Crushing minimizes the contribution of in situ produced isotopes and adsorbed atmospheric gases (Stuart et al. 1995; He et al. 2011). The detailed analytical and data processing procedures are described in He et al. (2011) and Su et al. (2014). Helium and Ar were introduced separately into the mass spectrometer and analyzed in static mode. Procedural blanks were run before each measurement. Both He and Ar blanks were negligible ($^3He < 3 \times 10^{-17}$ cc STP and $^{40}Ar < 4 \times 10^{-17}$ cc STP), about 0.1% of the signal from samples. The sample results were corrected for system blank and further calibrated by air shot and Helium HESJ standards (He Standard of Japan, $^3He/^4He = 20.63 \pm 0.10$ Ra, Matsuda et al. 2002).

In situ sulfur isotope analyses of pyrite

The sulfur isotope analyses of partial pyrite crystals from polished thin sections were performed on a Cameca IMS1280 secondary ion mass spectrometer (SIMS) at

IGGCAS. The analytical technique is described in detail in Chen et al. (2015) and Feng et al. (2018). The Cs^+ primary ion beam with an acceleration voltage of 10 kV and an intensity of ca. 2.5 nA was focused on ~ 10 × 15 μm oval area on the target pyrite. The well-characterized Sonora pyrite ($\delta^{34}S_{VCDT} = +1.61‰$ and $\delta^{33}S_{VCDT} = +0.83‰$, Farquhar et al. 2013) was used as a running standard for the calibration of $\delta^{34}S$. Two analyses of the standard were conducted approximately after each seven sample analyses.

Some pyrite crystals were analyzed in polished thin sections using a Nu Plasma II MC-ICP-MS, equipped with the 193-nm excimer ArF laser ablation system at GPMR, China University of Geosciences (Wuhan). The diameter of the laser beam was 33 μm with a repetition rate of 8 Hz and an energy fluency of 3–4 J/cm^2. Each data point was acquired for 40 s for the ^{34}S and ^{32}S isotopic species. An in-house pyrite standard named WS-1 ($\delta^{34}S_{V\text{-}CDT} = 0.9$) was used to correct the instrumental mass bias. The analytical precision is better than 0.5‰.

Results

Zircon U–Pb ages of Guojialing granodiorite, pegmatite, and mafic dykes

Zircon crystals from the Guojialing granodiorite (sample: 14DLH-01) are generally euhedral and display magmatic oscillatory growth zoning in cathodoluminescence (CL) images (Fig. 6a). Minor grains show core–rim textures, with well-defined oscillatory zoning in the rim, and bright and homogeneous core. A total of 19 spots were analyzed on the regions with oscillatory zoning. All analyses yield concordant results, with a weighted mean $^{206}Pb/^{238}U$ age of 129 ± 0.6 Ma (MSWD = 0.1; Fig. 6a), interpreted to be the crystallization age of the granodiorite. Two spots were conducted on the CL-bright cores, yielding $^{207}Pb/^{206}Pb$ ages of 2483 Ma and 2516 Ma (Supplementary Table 1), respectively. Thus, the CL-bright zircon cores are likely inherited from the basement of the Jiaobei Terrane.

Zircon grains from the granitic pegmatite dyke (sample 14DLH-34) are colorless to pale brown, and elongate and prismatic in shape. Most grains are dark and homogeneous in CL images (Fig. 6b), which is probably due to metamictization related to high U (4650–9672 ppm) and Th (1963–5126 ppm) concentrations (Supplementary Table 1). This is a typical feature for zircon from highly evolved magmatic rocks (Lupulscu et al. 2011). Minor grains show magmatic oscillatory zoning (Fig. 6b), with relatively low U (2170–3225 ppm) and Th (978–1558 ppm) concentrations. The analyses were conducted on both zircon domains, and their ages are almost indistinguishable. The analyses define a tight cluster at ca. 126 Ma along the Concordia line (Fig. 6b), with a weighted mean $^{206}Pb/^{238}U$ age of 126.2 ± 0.6 Ma (MSWD = 0.33, $N = 15$).

Zircon grains from a pre-ore mafic dyke (sample 14DLH-14, Fig. 7a) are generally euhedral–subhedral or irregular in shape. A total of 19 spots were analyzed on 18 zircons. Three grains without zoning under CL yield Paleoproterozoic $^{207}Pb/^{206}Pb$ ages, 2069 Ma, 1973 Ma, and 1776 Ma, which are considered inheritance from the basement of the Jiaobei terrain (Cai et al. 2013). Two similar grains show obvious discordant ages of 679 Ma and 1390 Ma, respectively, resulting from Pb loss. One grain with a core–rim texture has a $^{207}Pb/^{206}Pb$ age of 2417 Ma for the core and

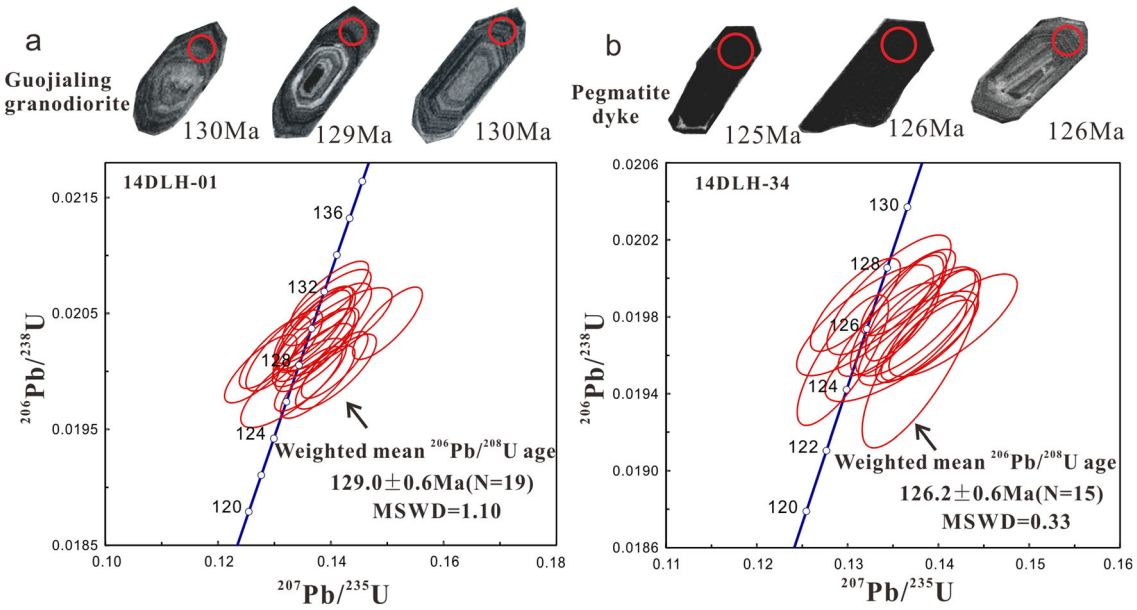

Fig. 6 Representative zircon crystals and U–Pb concordia diagram for Guojialing granodiorite (**a**) and pegmatite dyke (**b**), respectively

$^{206}Pb/^{238}U$ age of 158 Ma for the rim. This grain is thought to be assimilated from the Jurassic granitoids during the intrusion of the basic magma (Li et al. 2018). The remaining zircons generally show oscillatory growth zoning and can be divided into two groups (Supplementary Table 1 and Fig. 7c). The first group shows an age range of ca. 153–168 Ma ($^{206}Pb/^{238}U$), corresponding to those of the late Jurassic granitoids (Hou et al. 2007b; Yang et al. 2012; Li et al. 2018). They are considered to be assimilated during basic magma ascent. The second group grains have concordant and coherent ages, with a weighted mean $^{206}Pb/^{238}U$ age of 124.3 ± 1.5 Ma (MSWD = 0.19, $N = 5$) that marks the emplacement age of the mafic dyke.

Zircons from a syn-ore mafic dyke (sample 14HLG-06, Fig. 7b) in the adjacent Heilan'gou deposit (Fig. 1) are euhedral and show oscillatory growth zoning under CL images (Fig. 7d). One grain has a $^{206}Pb/^{238}U$ age of 158 Ma (Supplementary Table 1), which is likely incorporated from the late Jurassic granitoids. The other grains are concordant and yield a weighted mean $^{206}Pb/^{238}U$ age of 121.1 ± 0.7 Ma (MSWD = 0.62, $N = 20$), which is considered to be the emplacement age of the dyke.

Hydrothermal monazite U–Pb age

Monazite grains were selected from quartz-pyrite veins of stage II. The grains have anhedral morphology and appear homogeneous in BSE images. Most monazite occurs in fractures or as inclusions in pyrite and quartz (Fig. 5a, b), indicating that this hydrothermal monazite was deposited at the same time or shortly after pyrite and quartz. Overall, 31 spots were analyzed on the hydrothermal monazite grains (Supplementary Table 1). The analyses showed that most crystals contain common Pb, and thus the Tera–Wasserburg Concordia diagram (Tera and Wasserburg 1972) and a ^{207}Pb-based correction method were performed for common Pb

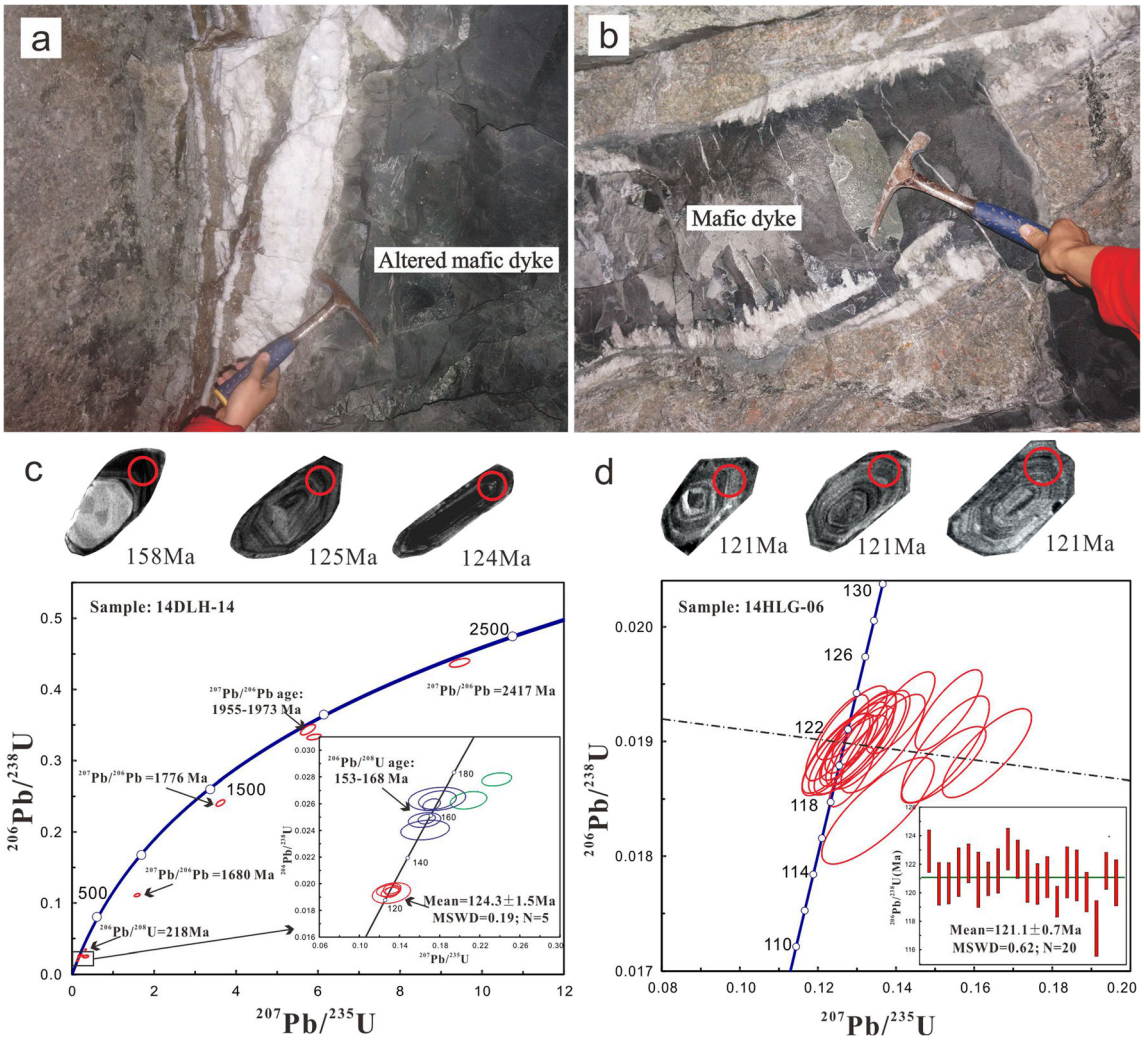

Fig. 7 Representative zircon crystals and U–Pb concordia diagram for the pre-ore altered mafic dyke (**a**, **c**) in the Daliuhang deposit and syn-ore mafic dyke (**b**, **d**) in the adjacent Heilan'gou deposit, respectively. Note that the unaltered mafic dykes are interleaved with auriferous quartz veins (**b**) in the mineralized fault zone, implying a close spatial and temporal relationship between the quartz veins and mafic dykes

correction. This approach has been shown to be effective in correcting common Pb in monazite (Storey et al. 2006; Chew et al. 2014; Jiang et al. 2016; Ma et al. 2017). On the Tera–Wasserburg diagram, the common Pb-uncorrected data define a linear array (Fig. 5c), giving a lower-intercept age at 120.5 ± 2.0 Ma (MSWD = 0.44). The *Y*-axis intercept of initial common $^{207}Pb/^{206}Pb$ ratios is 0.88 ± 0.03, which was used in the ^{207}Pb-based correction method to obtain the weighted mean $^{206}Pb/^{238}U$ age of all the analyzed crystals. The resultant age of 120.5 ± 1.7 Ma (MSWD = 0.52) (Fig. 5d) is almost indistinguishable from the lower-intercept age, indicating that the hydrothermal monazite formed at 120.5 Ma.

In situ Nd isotope of hydrothermal monazite

Hydrothermal monazite (Ce) crystals have $^{147}Sm/^{144}Nd$ ratios ranging from 0.1117 to 0.1185, and $^{143}Nd/^{144}Nd$ ratios from 0.51132 to 0.51136 (Supplementary Table 2). At the time of formation, the ε_{Nd} (t = 120 Ma) values of hydrothermal monazite would have ranged from − 13.7 to − 11.6, with an average value of − 12.8 (Fig. 8).

Helium–Ar isotopes of pyrite

The results of He and Ar isotope analyses of fluid inclusions in pyrite are listed in Supplementary Table 3 and illustrated in Fig. 9. The contents of ^{4}He are from 0.52×10^{-7} cm^3STPg^{-1} to 3.29×10^{-7} cm^3STPg^{-1}, and $^{3}He/^{4}He$ ratios range mainly from 1.13 to 1.50 Ra (average 1.32 Ra, except an anomalously low value of 0.14Ra). The concentrations of ^{40}Ar vary from 2.37×10^{-7} cm^3STPg^{-1} to 4.97×10^{-7} cm^3STPg^{-1}, with $^{40}Ar/^{36}Ar$ ratios in the range of 327–574, with 411 on average. The $^{3}He/^{36}Ar$ values are from 0.76×10^{-4} to 5.45×10^{-4}.

Sulfur isotope composition of pyrite

The sulfur isotope compositions of sulfide minerals from different rock types were obtained, including six ratios for pyrite from pegmatites, seven ratios for pyrite from K-feldspar-alteration zones, five ratios for Py1, 13 ratios for Py2, 14 ratios for Py2-altered, 26 ratios for Py3, and four ratios for Py4. Overall, pyrite crystals from different rock types have a narrow variation of $\delta^{34}S$ values (3.7–8.3‰, Fig. 10). Specifically, pyrite crystals from pegmatites and K-feldspar-alteration zones have the same mean $\delta^{34}S$ values of 7.1‰, but the latter domain shows a wide range (6.2‰ to 7.8‰) relative to the former domain (6.8‰ to 7.3‰). The $\delta^{34}S$ values of Py2 range from 6.7 to 7.5‰ (mean 7.1‰), similar to that of Py2-altered (6.8–7.5‰, mean 7.1‰). Py3 has the highest $\delta^{34}S$ values of 7.8‰ to 8.3‰, with a mean value of 8.0‰. Compared with the abovementioned pyrite domains, the early Py1 and late Py4 have distinctly lower $\delta^{34}S$ values from 3.7 to 5.6‰ (mean 4.6‰) and 5.3 to 6.4‰ (mean 5.9‰), respectively. Notably, there are grain-scale variations in $\delta^{34}S$ in pyrite grains from stage III (Fig. 4e, f). As shown in Fig. 4e, the core (Py2-altered) has $\delta^{34}S$ values of 6.8–6.9‰, with an increase to 7.9–8.1‰ on the rim (Py3). This is in good agreement with the results obtained by LA-MC-ICPMS on another pyrite grain (Fig. 4f).

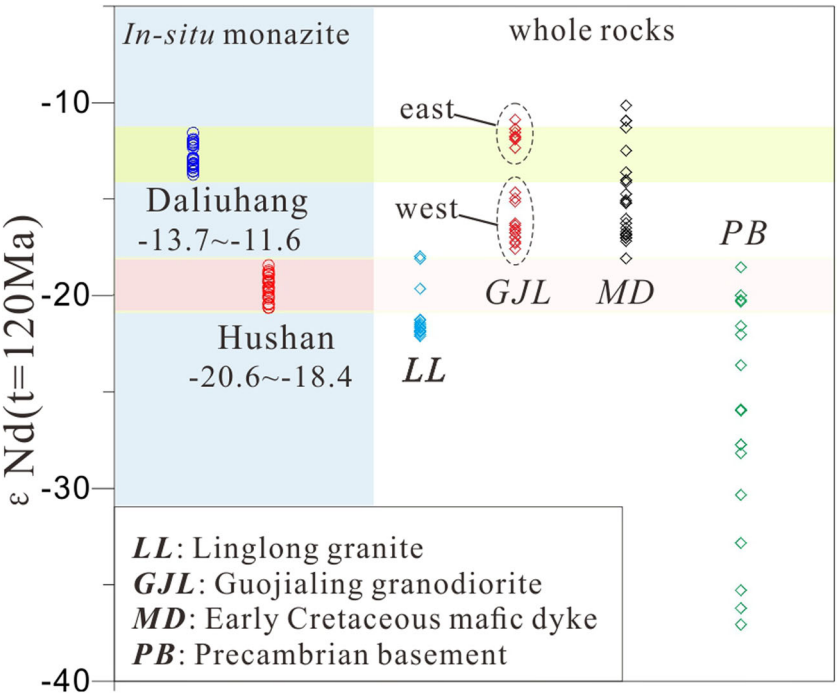

Fig. 8 A comparison diagram of the in situ monazite Nd isotopes in the Daliuhang ore bodies and whole-rock Nd isotopes of other typical units in the Jiaodong Peninsula, all calculated at 120 Ma. Note that the Nd isotopes of the eastern Guojialing granodiorite (located in the Penglai-Qixia belt) are more similar to the monazite from Daliuhang than the western part. Data from Yang et al. (2003, 2004); Hou et al. (2007b); Jahn et al. (2008); Yang et al. (2012); Cai et al. (2013); Ma et al. (2016); and this study

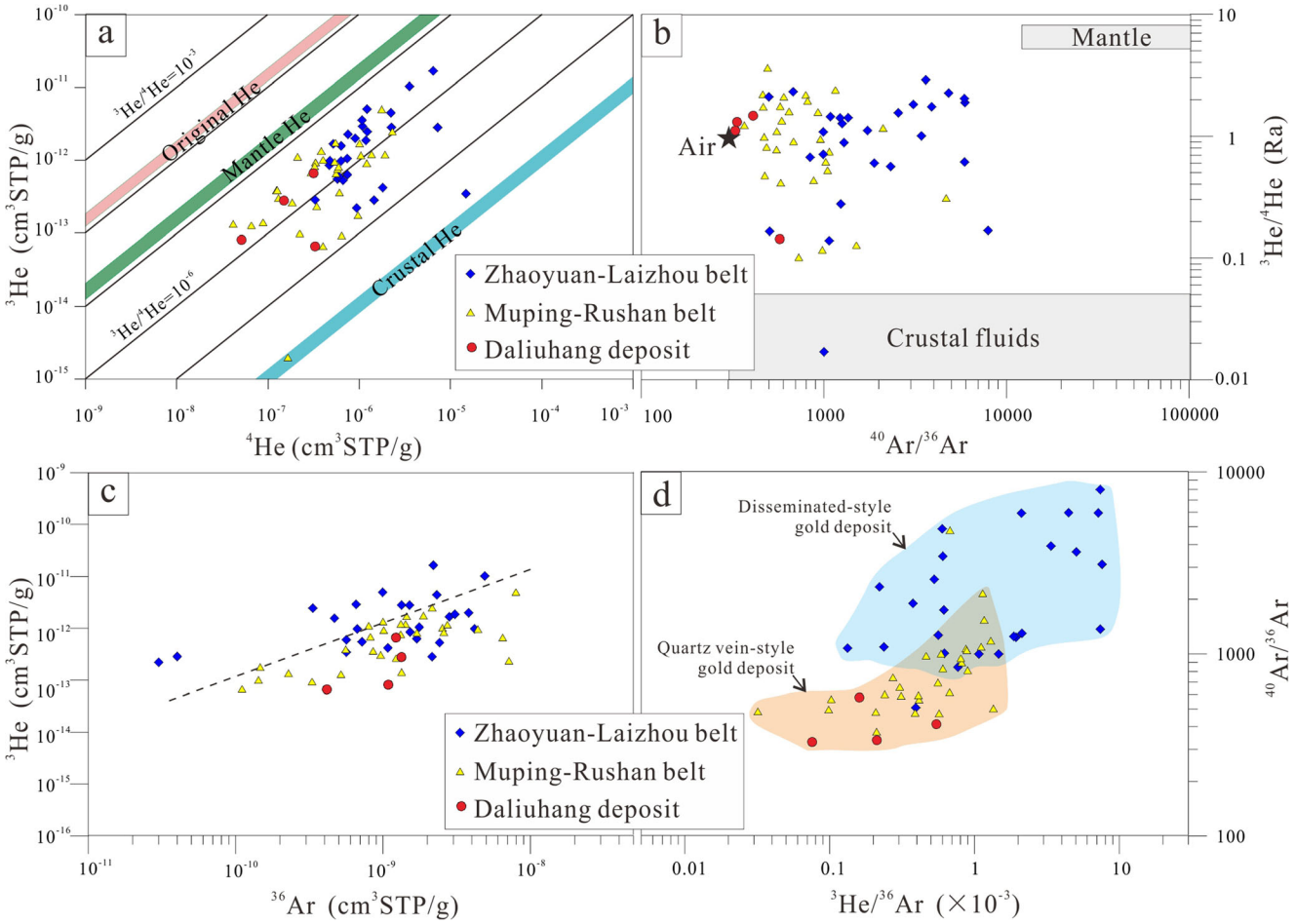

Fig. 9 Plots of **a** ^{3}He versus ^{4}He of fluid inclusions in pyrite from the Daliuhang deposit and other deposits in the Zhaoyuan-Laizhou belt and the Muping-Rushan belt; **b** ^{3}He/^{4}He versus ^{40}Ar/^{36}Ar; and **c** ^{3}He versus ^{36}Ar of fluid inclusions, showing a broadly positive correlation between these two isotopes. **d** Plot of ^{40}Ar/^{36}Ar versus ^{3}He/^{36}Ar, showing the relatively lower ^{40}Ar/^{36}Ar and ^{3}He/^{36}Ar ratios of quartz vein–style gold deposits relative to those of disseminated-style gold deposits. Data from Zhang et al. (2008); Zhang et al. (2012); Shen et al. (2013); Xue et al. (2013); Wen et al. (2016); Tan et al. (2018); and this study

Discussion

Relationship between gold mineralization and ore-hosting intrusions

A possible genetic association between gold mineralization and Late Mesozoic granitoids has been discussed for many years, largely due to their close spatial and broadly temporal association (Fan et al. 2007; Yan et al. 2014; Yang et al. 2014; Groves and Santosh 2015; Ma et al. 2017; Cai et al. 2018). The LA-ICP-MS zircon U–Pb ages of 129.0 ± 0.6 Ma for the ore-hosting Guojialing granodiorite in this study agree well with previous geochronological studies (Hou et al. 2007b; Yang et al. 2012; Li et al. 2018). The U–Pb age of a pegmatite dyke (126.2 ± 0.6 Ma) in the mining district indicates a slightly younger emplacement age than the Guojialing granodiorite. Hydrothermal monazite dating indicates that the gold mineralization in the Daliuhang deposit occurred at 120.5 ± 1.7 Ma, which is also in agreement with the U–Pb ages of syn-ore mafic dykes (121.1 ± 0.7 Ma, Fig. 7b) in the adjacent Heilan'gou deposit. The newly obtained mineralization age lies within the broad range of 126 to 117 Ma for previous estimates of gold mineralization in the Jiaodong Peninsula (Fan et al. 2007, 2016; Ma et al. 2017; Cai et al. 2018).

The above robust dating results show a measurable age gap between the ore-hosting intrusion solidification and gold deposition, such that gold mineralization cannot have a direct association with granite magmatism. This is also supported by the ^{40}Ar/^{39}Ar ages of pristine biotite from Guojialing granodiorites (124.5–124.0 Ma, Li et al. 2003), indicating that the intrusions had cooled below ~ 350 °C before gold mineralization. The lack of ore-element and temperature-related alteration zonation around the intrusions further negates a magmatic-hydrothermal model by comparison with known intrusion-related gold systems (Lang and Baker 2001; Sillitoe 2008). The contacts between granitic intrusions and Precambrian basement rocks are particularly favorable sites for mineralization, with heterogeneous stress and

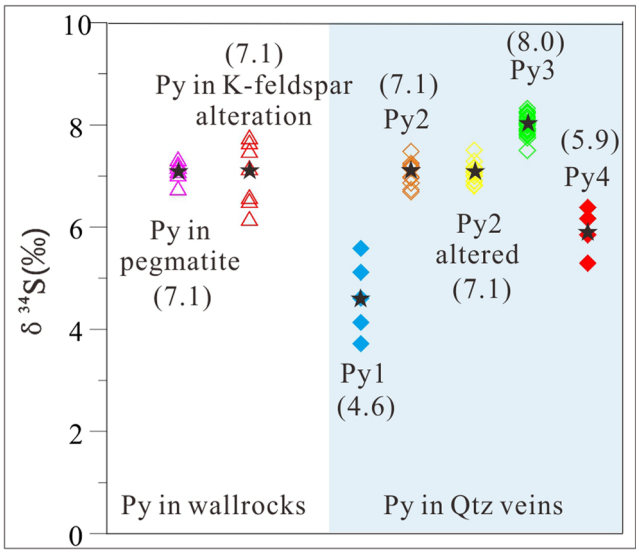

Fig. 10 Variations in sulfur isotope compositions of various generations of pyrite in the Daliuhang deposit, with the mean $\delta^{34}S$ values for each type

inhomogeneous strain between different rock units focusing ore-fluid infiltration (Groves et al. 2018) within the controlling fault zone. It is significant that some unaltered syn-ore mafic dykes are interleaved with auriferous quartz veins within the same fault zone (Fig. 7b) in the adjacent Heilan'gou deposit. Given the spatial and temporal association between gold mineralization and mantle-derived mafic rocks (Fig. 7), the ore-controlling faults are inferred to have great vertical depth extension (Zhao et al. 2012) and to have facilitated the advection of deeply sourced fluids to the site of gold mineralization at shallower crustal levels.

Origin of ore-forming fluids

Pyrite is known to be a suitable trap for noble gases (Kendrick et al. 2001), with previous work showing that the effect of noble-gas diffusive loss on the He–Ar isotopic radio is almost negligible (Hu et al. 1998; Kendrick et al. 2001; Tan et al. 2018). Although in situ production of ^{4}He and ^{40}Ar due to radioactive decay of U–Th and K in fluid inclusions may be superimposed on the primary noble-gas compositions, this problem can be effectively avoided by multi-step crushing extractions (He et al. 2011; Su et al. 2014). Thus, the measured He–Ar isotopes are interpreted to represent the compositions of primary fluids trapped in pyrite.

The measured $^{3}He/^{36}Ar$ ratios (0.76×10^{-4}–5.45×10^{-4}) are much higher than those of atmosphere or air-saturated water (5×10^{-8}), indicating that the fluids contain negligible atmospheric He (Kendrick et al. 2001). On a ^{3}He versus ^{4}He plot, samples from the Daliuhang deposit lie between the crustal and mantle curves (Fig. 9a, b), indicating mixed sources between those two reservoirs. The proportions of mantle and crustal contributions are crucial for understanding fluid origin, and can be calculated from the following equation:

$$He_{mantle}\ (\%) = (R_S – R_C)/(R_M – R_C) \times 100$$

In which R_M, R_C (= 0.03), and R_S (= 1.32) represent $^{3}He/^{4}He$ ratios of mantle, crust, and sample, respectively. Typical subcontinental lithospheric mantle (SCLM) has higher $^{3}He/^{4}He$ ratios of ~6–7 Ra (Dunai and Baur 1995; Gautheron and Moreira 2002) than crust (0.01–0.05 Ra; Mamyrin and Tolstikhin 2013). However, Tan et al. (2018) recently estimated that the lithospheric mantle below the eastern North China Craton has $^{3}He/^{4}He$ ratios of 3.3–4.0 Ra, probably due to subduction-related metasomatism. Su et al. (2014) also obtained similar low $^{3}He/^{4}He$ ratios (down to 2.3 Ra) for pyroxene from mantle xenoliths derived from beneath the Jiaodong Peninsula. According to their results, 7.0 and 3.3 were selected as the maximum and minimum R_M, respectively. As a result, the mantle contribution from the current study is estimated to be between 20 and 40%.

In terms of possible sources of the crustal-component of the ore-forming fluids, the $^{40}Ar/^{36}Ar$ ratios (327–574) of fluids in pyrite are much lower than those of deeply derived mantle fluids (≥ 12,000, Burnard et al. 1997; 30,000–40,000, Kendrick and Burnard 2013), but slightly higher than the atmospheric value of 295.5, which indicates a significant influence of atmospheric compositions. Possible explanations for atmospheric contamination include the following: (1) involvement of ancient meteoric water, (2) current atmospheric contamination during sample preparation or measurement, (3) influence of secondary fluid inclusions unrelated to gold ore formation, and (4) the addition of an atmosphere-derived Ar component into the mantle through subduction. Previous fluid inclusion thermobarometric results indicate that the Daliuhang deposit was formed at an estimated 1.9–3.0 kbar, corresponding to depths of 7–11 km under a lithostatic load (Li et al. 2018), which precludes an influx of meteoric water into the fluid system at such deep levels (Goldfarb and Groves 2015). Modern atmospheric contamination has been avoided by careful washing, extended baking under vacuum, and a crushing technique to release gas from fluid inclusions in this study (He et al. 2011; Guo et al. 2018). However, the effects of undetectable secondary fluid inclusions within pyrite cannot be dismissed. Other quartz vein–style deposits in the Jiaodong Peninsular have similar $^{40}Ar/^{36}Ar$ ratios (mainly in the range of 367–1507, Zhang et al. 2012; Xue et al. 2013; Tan et al. 2018, Fig. 9d), although the disseminated-style deposits generally have higher ratios (mainly in the range of 840–3895, Zhang et al. 2008; Shen et al. 2013; Wen et al. 2016). There is no evidence to indicate that the quartz vein–style deposits are more influenced by post-ore secondary inclusions than the disseminated-style deposits. Thus, it is inferred that the effect

of post-ore secondary inclusions is not the major factor producing the atmosphere-like Ar isotopic signatures.

In addition, there is a broadly positive correlation between ^{36}Ar and ^{3}He (Fig. 9c). The ^{3}He and ^{36}Ar are both non-radiogenic and suggest sources from the mantle and the atmosphere, respectively. The most logical interpretation is that there has been addition of an atmospheric noble-gas component into the mantle through subduction (Matsumoto et al. 2001; Gautheron et al. 2005; Hopp and Ionov 2011; Broadley et al. 2016). Therefore, it is deduced that ore fluids were derived via devolatilization of the sedimentary wedge, with its atmospheric component, and oceanic crust or overlying mantle lithosphere during subduction of the paleo-Pacific plate beneath the eastern North China Craton in the early Cretaceous (Zhai and Santosh 2013; Zhu et al. 2011; Goldfarb and Santosh 2014; Goldfarb and Groves 2015 and references therein). With respect to those relatively high $^{40}Ar/^{36}Ar$ ratios in most disseminated-style deposits, a logical explanation would be the introduction of more crustal contents ($^{40}Ar/^{36}Ar$ value, 299–100,000, Kendrick and Burnard 2013) via more intense fluid/rock interaction than for the vein-style deposits.

Source of sulfur and ore metals

The sulfur isotope ratios of sulfides that co-precipitated with gold have been utilized as a reliable tool to deduce the source of gold, as it commonly complexes with bisulfide as $Au(HS)_2^-$ in hydrothermal fluids (Hayashi and Ohmoto 1991; Benning and Seward 1996; Stefansson and Seward 2004; Williams-Jones et al. 2009). There is a narrow variation of $\delta^{34}S$ values (3.7–8.3‰) at Daliuhang, basically similar to other deposits in the Jiaodong gold district (Hou et al. 2007a; Yan et al. 2014; Wang et al. 2015; Wen et al. 2016; Feng et al. 2018; Yang et al. 2018). In concert with the noble-gas data, these positive $\delta^{34}S$ values are consistent with a model in which some sulfur was derived from mantle-crustal mixing processes at depth related to devolatilization during subduction of the paleo-Pacific plate (Deng et al. 2015; Zhu et al. 2015; Goldfarb and Groves 2015). However, it is inevitable that such fluids would scavenge additional sulfur from upper crustal rocks during advection, making it difficult to unequivocally define the ultimate fluid source. Due to the low percentage of sulfide assemblages that include pyrite, galena, sphalerite, and chalcopyrite, in the Daliuhang deposit, the ore-forming fluids are interpreted to have contained relatively low H_2S contents. Given the range of $\delta^{34}S$ values, the influence of precipitation of mineral phases on the $\delta^{34}S$ values of the ore fluids should be taken into account when interpreting these values (Ohmoto 1972; Zheng and Hoefs 1993). The newly reported experimental equilibrium $^{34}S/^{32}S$ fractionation between pyrite and H_2S is − 1.9‰ (Syverson et al. 2015), which means that the precipitation of pyrite from a closed-solution system would lead to an increase in the $\delta^{34}S$ value of sulfur remaining in the solution with time.

The early-stage fluid in equilibrium with pre-ore Py1 has relatively low $\delta^{34}S$ values ranging from 5.6 to 7.5‰ (mean of 6.5‰), which are broadly similar to those of pyrite from distal K-feldspar alteration ($\delta^{34}S$ = 6.2–7.8‰, mean 7.1‰). The ore-hosting Guojialing granodiorite has comparable isotope compositions ($\delta^{34}S$ = 2.7–10.0‰, average 6.7‰; Wang et al. 2002), which are consistent with the $\delta^{34}S$ values of pyrite crystals from pegmatites ($\delta^{34}S$ = 6.8–7.3‰, average 7.1‰). These similar sulfur isotopic compositions imply considerable isotope exchange between early-stage fluids and host rocks.

Compared with early-stage Py1, ore-related pyrites (Py2 and Py3) have higher $\delta^{34}S$ values (6.7–8.3‰), with corresponding calculated $\delta^{34}S$ values of 8.6–10.2‰ for ore-forming fluids. Phase separation triggered by pressure fluctuation during fault movement is considered a critical mechanism for gold deposition in the Jiaodong gold deposits (Hou et al. 2007a; Wen et al. 2015; Wang et al. 2015; Yang et al. 2016; Li et al. 2018). During phase separation, reduced gases, such as H_2, CH_4, and H_2S, preferentially partition into the vapor phase, and may cause an increase in S^{+6}/S^{-2} and result in relatively oxidized residual fluids (Drummond and Ohmoto 1985; Weatherley and Henley 2013). If so, the resultant pyrite would have lower, or even negative, $\delta^{34}S$ values (Mckibben and Eldridge 1990; Hodkiewicz et al. 2009; Peterson and Mavrogenes 2014), which is opposite to the trend in this study. Considering the limited amount of Py1, mass fractionation during precipitation of pyrite seems unable to explain such elevated $\delta^{34}S$ values. In this case, an external ^{34}S-enriched source appears to be required. Previous studies have measured the bulk sulfur isotopic compositions of Jiaodong Group metamorphic rocks (− 1.3–7.8‰, mean 5.0‰; Wang et al. 2002), Jingshan Group meta-volcanic-sedimentary rocks (8.2–12.0‰, average 9.7‰; Zhang and Chen 1999), and mafic dykes (5.3–10.8‰, average 6.9‰; Huang 1994). From these data, it is inferred that some sulfur from the Jingshan Group was leached into the ore-forming system. This interpretation is also supported by elevated As concentrations of ore-related pyrite (Feng et al. 2018 and our unpublished data), with As commonly enriched in meta-sedimentary rocks (mean 3.32 ppm) relative to Guojialing granodiorite (mean 0.25 ppm) and Linglong granites (mean 0.38 ppm) as determined by Ding et al. (1997).

Additionally, within the ore-related stages, there is a relative increase in $\delta^{34}S$ values from Py2 to Py3 (Fig. 10), which is consistent with variations from core to rim within individual pyrites (Fig. 6e, f). Such variations may reflect the collective influence of mass fractionation, precipitation of earlier Py2 grains, and involvement of an external ^{34}S-enriched source. Subsequently, base-metal sulfides are deposited, consuming the remaining sulfur in solution, resulting in deposition of

native gold intergrown with other sulfide minerals (Fig. 4d). In stage IV, with decrease of temperature and H_2S activity, there are only minor amounts of pyrite with lower ^{34}S precipitated.

Source of REE

Hydrothermal monazite has initial Nd isotopic compositions overlapping those of the ore-hosting Guojialing granodiorite (Fig. 8). Thus, rare earth element (REE) components in the ore-forming fluids were most likely extracted from the Guojialing intrusions along the fluid flow path. At a broader scale, the Sr and Nd isotope ratios of ore-related hydrothermal minerals from other gold deposits in the region also overlap with those of their corresponding host units (Li et al. 2013; Yang et al. 2018). The ore-forming fluids that formed the Jiaodong deposits are characterized by lower REE concentrations (bulk of sulfide ores in the Xinli gold deposit: ΣREE = 26–190 ppm, average 71 ppm; Zhao et al. 2015) than the Guojialing granodiorites (ΣREE = 125–770 ppm, average 309 ppm; Li et al. 2019). This interpretation is consistent with the rarity of REE-bearing minerals (mainly minor monazite) in most thin sections of the gold ores. Thus, the Nd isotope ratios of ore-forming fluids are sensitive to input of REE from wall rocks via fluid–rock interaction.

Implications for ore genesis

Gold deposits in the Jiaodong province display many characteristics, such as ore-controlling fault systems, fluid inclusion compositions, stable isotope chemistry, and ore and alteration mineral assemblages, similar to orogenic gold deposits worldwide, but regional metamorphism in the region was two billion years prior to gold mineralization, negating a classical crustal metamorphic model for their genesis (Fan et al. 2007, 2016; Li et al. 2013; Zhai and Santosh 2013; Goldfarb and Santosh 2014; Ma et al. 2017). As discussed above, a magmatic-hydrothermal model for mineralization is also not supported by available field and geochronological evidence. Groves and Santosh (2015) proposed a unified model for orogenic gold deposits, in which the gold is derived from devolatilization of stalled subduction plates and overlying oceanic sediments, which have been demonstrated to be important carriers of Au, As, and S (Bierlein and Craw 2009; Large et al. 2014; Pitcairn et al. 2015). In support of such a model, the newly obtained noble-gas data, together with previous results, indicate that devolatilization of the paleo-Pacific slab and sediment slab, combined with interaction with mantle lithosphere, was the source of initial ore fluids and at least some ore metals. These deeply sourced fluids migrated along deep-seated faults (the western Tan-Lu Fault up to 70 km deep, equivalent to an upper mantle level, Ren et al. 1997; Li et al. 2003; Zhao et al. 2012; Zhu et al. 2015), which were also conduits for widespread, pene-contemporaneous basic magmas that crystallized to form mafic dykes. During advection, the deep, original S- and REE-poor, ore fluids leached sulfur and REEs (especially Nd) from granitic host rocks and meta-sedimentary rocks in the upper crust.

Conclusions

The U–Pb age of 120.5 ± 1.7 Ma for hydrothermal monazite represents the timing of gold mineralization at the Daliuhang gold deposit. It places the age of gold mineralization at least five million years younger than the latest granitic magmatic activity indicated by the ca. 126 Ma age of pegmatite dykes that intruded the ca. 129 Ma ore-hosting Guojialing granodiorite. Therefore, a genetic relationship between gold mineralization and early Cretaceous magmatic-hydrothermal activity is negated. Noble-gas isotope ratios are consistent with a model in which ore-forming fluids were initially derived from devolatilization of the subducted slab and overlying sediment wedge and interaction with overlying mantle lithosphere during paleo-Pacific plate subduction in the early Cretaceous. The deeply sourced fluids migrated upwards along crustal-scale faults, defined by the occurrence of widespread mafic dykes, scavenging sulfur and REEs from upper crustal rocks into the ore fluid, thus creating mixed mantle-crustal signatures in isotopic ratios of ore minerals and fluid inclusions within them. During the main ore stage, gold was initially incorporated into arsenian pyrite, but later was deposited as native gold as sulfur activity decreased in an already low-S fluid.

Acknowledgements Drs. Xin Yan, Kuidong Zhao, Yueheng Yang, and Guoqiang Tang are thanked for their technical supports during analyses of the SEM, LA-ICPMS, LA-MC-ICPMS, and SIMS, respectively. Dr. Xiaochun Li is thanked for the helpful suggestions improving an early version of this manuscript. Drs Pete Hollings and Thomas Ulrich are thanked for their constructive and valuable comments which greatly contributed to improvement of the manuscript.

Funding information This research was jointly supported by the National Key Research and Development Program (no. 2016YFC0600105) and the National Natural Science Foundation of China (41772080).

References

Aleinikoff JN, Schenck WS, Plank MO, Srogi L, Fanning CM, Kamo SL, Bosbyshell H (2006) Deciphering igneous and metamorphic events in high-grade rocks of the Wilmington Complex, Delaware: morphology, cathodoluminescence and backscattered electron zoning, and SHRIMP U-Pb geochronology of zircon and monazite. Geol SocAm Bull 118:39–64

Benning LG, Seward TM (1996) Hydrosulphide complexing of gold (I) in hydrothermal solutions from 150 to 500 °C and 500 to 1500 bars. Geochim Cosmochim Acta 60:1849–1871

Bierlein FP, Craw D (2009) Petrogenetic character and provenance of metabasalts in the Aspiring and Torlesse terranes, South Island, New Zealand: implications for the gold endowment of the Otago Schist. Chem Geol 260:301–315

Broadley MW, Ballentine CJ, Chavrit D, Dallai L, Burgess R (2016) Sedimentary halogens and noble gases within Western Antarctic xenoliths: implications of extensive volatile recycling to the sub continental lithospheric mantle. Geochim Cosmochim Acta 176: 139–156

Burnard P, Graham D, Turner G (1997) Vesicle-specific noble gas analyses of "popping rock": implications for primordial noble gases in earth. Science 276:568–571

Cai YC, Fan HR, Santosh M, Liu X, Hu FF, Yang KF, Lan TG, Yang YH, Liu YS (2013) Evolution of the lithospheric mantle beneath the southeastern North China Craton: constraints from mafic dikes in the Jiaobei terrain. Gondwana Res 24:601–621

Cai YC, Fan HR, Santosh M, Hu FF, Yang KF, Li XH (2018) Decratonic gold mineralization: evidence from the Shangzhuang gold deposit, eastern North China Craton. Gondwana Res 54:1–22

Chang JS, Zhang GD, Cai XN, Guo LH (2013) Control action of mixed igneous complex to the natural gold deposits of Qi-Peng Gold Min, Shandong Province. Gold Sci Technol 21:20–27 (in Chinese with English abstract)

Chen L, Li XH, Li JW, Hofstra AH, Liu Y, Koenig AE (2015) Extreme variation of sulfur isotopic compositions in pyrite from the Qiuling sediment-hosted gold deposit, West Qinling orogen, central China: an in situ SIMS study with implications for the source of sulfur. Mineral Deposita 50:643–656

Chew DM, Petrus JA, Kamber BS (2014) U–Pb LA–ICPMS dating using accessory mineral standards with variable common Pb. Chem Geol 363:185–199

Deng J, Liu XF, Wang QF, Pan RG (2015) Origin of the Jiaodong-type Xinli gold deposit, Jiaodong Peninsula, China: constraints from fluid inclusion and C–D–O–S–Sr isotope compositions. Ore Geol Rev 65:674–686

Ding SJ, Zhai YS, Deng J (1997) Geology and geochemical study on gold potentiality of geological units in east Shandong. Contrib Geol Miner Resour Res 3:1–10 (in Chinese with English abstract)

Drummond SE, Ohmoto H (1985) Chemical evolution and mineral deposition in boiling hydrothermal systems. Econ Geol 80:126–147

Dunai T, Baur H (1995) Helium, neon, and argon systematics of the European subcontinental mantle: implications for its geochemical evolution. Geochim Cosmochim Acta 59:2767–2783

Fan HR, Hu FF, Yang JH, Zhai MG (2007) Fluid evolution and large-scale gold metallogeny during Mesozoic tectonic transition in the Jiaodong Peninsula, eastern China. Geol Soc Lond, Spec Publ 280: 303–316

Fan HR, Feng K, Li XH, Hu FF, Yang KF (2016) Mesozoic gold mineralization in the Jiaodong and Korean peninsulas. Acta Petrol Sin 32: 3225–3238 (in Chinese with English abstract)

Farquhar J, Cliff J, Zerkle AL, Kamyshny A, Poulton SW, Claire M, Adams D, Harms B (2013) Pathways for Neoarchean pyrite formation constrained by mass independent sulfur isotopes. Proc Natl Acad Sci U S A 110:17638–17643

Feng K, Fan HR, Hu FF, Yang KF, Liu X, Shangguan YN, Jiang P (2018) Involvement of anomalously As-Au-rich fluids in the mineralization of the Heilan'gou gold deposit, Jiaodong, China: evidence from trace element mapping and in-situ sulfur isotope composition. J Asian Earth Sci 160:304–321

Gautheron C, Moreira M (2002) Helium signature of the subcontinental lithospheric mantle. Earth Planet Sci Lett 199:39–47

Gautheron C, Moreira M, Allegre C (2005) He, Ne and Ar composition of the European lithospheric mantle. Chem Geol 217:97–112

Goldfarb RJ, Santosh M (2014) The dilemma of the Jiaodong gold deposits: are they unique? Geosci Front 5:139–153

Goldfarb RJ, Groves DI (2015) Orogenic gold: common or evolving fluid and metal sources through time. Lithos 233:2–26

Griffin WL, Powell WJ, Pearson NJ, O'Reilly SY (2008) GLITTER: data reduction software for laser ablation ICP-MS Laser Ablation-ICP-MS in the earth sciences. Mineral Assoc Canada Short Course Series 40:204–207

Groves DI, Santosh M (2015) The giant Jiaodong gold province: the key to a unified model for orogenic gold deposits. Geosci Front 7:409–417

Groves DI, Santosh M, Goldfarb RJ, Zhang L (2018) Structural geometry of orogenic gold deposits: implications for exploration of world-class and giant deposits. Geosci Front 9:1163–1177

Guo W, He HY, Hilton DR, Zheng YF, Su F, Liu Y, Zhu RX (2018) Recycled noble gases preserved in podiform chromitites from Luobusa, Tibet. Chem Geol 469:97–109

Hayashi KI, Ohmoto H (1991) Solubility of gold in NaCl- and H_2S-bearing aqueous solutions at 250–350 °C. Geochim Cosmochim Acta 55:2111–2126

He HY, Zhu RX, Saxton J (2011) Noble gas isotopes in corundum and peridotite xenoliths from the eastern North China Craton: implication for comprehensive refertilization of lithospheric mantle. Phys Earth Planet Inter 189:185–191

Hodkiewicz PF, Groves DI, Davidson GJ, Weinberg RF, Hagemann SG (2009) Influence of structural setting on sulphur isotopes in Archean orogenic gold deposits, Eastern Goldfields Province, Yilgarn, Western Australia. Mineral Deposita 44:129–150

Hopp J, Ionov DA (2011) Tracing partial melting and subduction-related metasomatism in the Kamchatkan mantle wedge using noble gas compositions. Earth Planet Sci Lett 302:121–131

Hou ML, Jiang SY, Shen K, Lian GJ, Liu QC, Xiao FL (2007a) Fluid inclusion and H-O isotope study of gold mineralization in the Penglai gold field, Eastern Shangdong. Acta Petrol Sin 23:2241–2256 (in Chinese with English abstract)

Hou ML, Jiang YH, Jiang SY, Ling HF, Zhao KD (2007b) Contrasting origins of late Mesozoic adakitic granitoids from the northwestern Jiaodong Peninsula, east China: implications for crustal thickening to delamination. Geol Mag 144:619–631

Hu RZ, Burnard PG, Turner G, Bi XW (1998) Helium and argon systematics in fluid inclusions of Machangqing copper deposit in west Yunnan province, China. Chem Geol 146:55–63

Huang DY (1994) Sulfur isotope studies of the metallogenic series of gold deposits in Jiaodong (East Shandong) area. Mineral Deposits 13:75–87 (in Chinese with English abstract)

Jahn BM, Liu DY, Wan YS, Song B, Wu JS (2008) Archean crustal evolution of the Jiaodong Peninsula, China, as revealed by zircon SHRIMP geochronology, elemental and Nd-isotope geochemistry. Am J Sci 308:232–269

Jiang P, Yang KF, Fan HR, Liu X, Cai YC, Yang YH (2016) Titanite-scale insights into multi-stage magma mixing in Early Cretaceous of NW Jiaodong terrane, North China Craton. Lithos 258:197–214

Kendrick MA, Burgess R, Pattrick RAD, Turner G (2001) Fluid inclusion noble gas and halogen evidence on the origin of cu-porphyry mineralising fluids. Geochim Cosmochim Acta 65:2651–2668

Kendrick MA, Burnard PG (2013) Noble gases and halogens in fluid inclusions: a journey through the earth's crust. In: The Noble Gases as Geochemical Tracers, pp: 319–369

Lang JR, Baker T (2001) Intrusion-related gold systems: the present level of understanding. Mineral Deposita 36:477–489

Large RR, Halpin JA, Danyushevsky LV, Maslennikov VV, Bull SW, Long JA, Gregory DD, Lounejeva E, Lyons TW, Sack PJ (2014) Trace element content of sedimentary pyrite as a new proxy for deep-time ocean–atmosphere evolution. Earth Planet Sci Lett 389: 209–220

Li JW, Vasconcelos PM, Zhang J, Zhou MF, Zhang XJ, Yang FH (2003) $^{40}Ar/^{39}Ar$ constraints on a temporal link between gold mineralization, magmatism, and continental margin transtension in the Jiaodong Gold Province, eastern China. J Geodyn 111:741–751

Li XC, Fan HR, Santosh M, Hu FF, Yang KF, Lan TG (2013) Hydrothermal alteration associated with Mesozoic granite-hosted gold mineralization at the Sanshandao deposit, Jiaodong Gold Province, China. Ore Geol Rev 53:403–421

Li XH, Fan HR, Zhang YW, Hu FF, Yang KF, Liu X, Zhao KD (2018) Rapid exhumation of the northern Jiaobei Terrane, North China Craton in the Early Cretaceous: insights from Al-in-hornblende barometry and U-Pb geochronology. J Asian Earth Sci 160:365–379

Li XH, Fan HR, Hu FF, Hollings P, Yang KF, Liu X (2019) Linking lithospheric thinning and magmatic evolution of late Jurassic to early cretaceous granitoids in the Jiaobei Terrane, southeastern North China craton. Lithos 324-325:280–296

Liu S, Hu RZ, Gao S, Feng CX, Yu BB, Qi YQ, Wang T, Feng GY, Coulson IM (2009) Zircon U-Pb age, geochemistry and Sr–Nd–Pb isotopic compositions of adakitic volcanic rocks from Jiaodong, Shandong Province, Eastern China: constraints on petrogenesis and implications. J Asian Earth Sci 35:445–458

Liu X, Fan HR, Evans NJ, Yang KF, Danišík M, McInnes BI, Qin K, Yu XF (2017) Exhumation history of the Sanshandao Au deposit, Jiaodong: constraints from structural analysis and (U-Th)/He thermochronology. Sci Rep 7:77–87

Liu ZC, Wu FY, Yang YH, Yang JH, Wilde SA (2012) Neodymium isotopic compositions of the standard monazites used in U-Th-Pb geochronology. Chem Geol 334:221–239

Liu YS, Hu ZC, Zong KQ, Gao CG, Gao S, Xu J, Chen HH (2010) Reappraisement and refinement of zircon U-Pb isotope and trace element analyses by LA-ICP-MS. Chin Sci Bull 55:1535–1546

Lupulscu MV, Chiarenzelli JR, Pullen AT, Price JD (2011) Using pegmatite geochronology to constrain temporal events in the Adirondack Mountains. Geosphere 7:23–39

Ma L, Jiang SY, Hofmann AW, Xu YG, Dai BZ, Hou ML (2016) Rapid lithospheric thinning of the North China Craton: new evidence from cretaceous mafic dikes in the Jiaodong Peninsula. Chem Geol 432:1–15

Ma WD, Fan HR, Liu X, Pirajno F, Hu FF, Yang KF, Yang YH, Xu WG, Jiang P (2017) Geochronological framework of the Xiadian gold deposit in the Jiaodong province, China: implications for the timing of gold mineralization. Ore Geol Rev 86:196–211

Mamyrin BA, Tolstikhin I (2013) Helium isotopes in nature. Elsevier Science Publishers, New York, pp 203–207

Matsuda J, Matsumoto T, Sumino H, Nagao K, Yamamoto J, Miura Y, Kaneoka I, Takahata N, Sano Y (2002) The $^{3}He/^{4}He$ ratio of the new internal He standard of Japan (HESJ). Geochem J 36:191–195

Matsumoto T, Chen Y, Matsuda JI (2001) Concomitant occurrence of primordial and recycled noble gases in the Earth's mantle. Earth Planet Sci Lett 185:35–47

McKibben MA, Eldridge CS (1990) Radical sulfur isotope zonation of pyrite accompanying boiling and epithermal gold deposition; a SHRIMP study of the Valles Caldera, New Mexico. Econ Geol 85:1917–1925

Miao LC, Luo ZK, Huang JZ, Guan K, Wang LG, McNaughton NJ, Groves DI (1997) Zircon SHRIMP study of granitoid intrusions in Zhaoye gold belt of Shandong province and its implication. Sci China Ser D: Earth Science 40:361–369

Ohmoto H (1972) Systematics of sulfur and carbon isotopes in hydrothermal ore deposits. Econ Geol 67:551–578

Peterson EC, Mavrogenes JA (2014) Linking high-grade gold mineralization to earthquake-induced fault-valve processes in the Porgera gold deposit, Papua New Guinea. Geology 42:383–386

Pitcairn IK, Craw D, Teagle DAH (2015) Metabasalts as sources of metals in orogenic gold deposits. Mineral Deposita 50:373–390

Ren YS, Lin G, Peng XL (1997) Controlling of Tanlu fault system on gold deposits in the western part of Jiaodong area, Shandong Province. Gold 2:3–7 (in Chinese with English abstract)

Shen JF, Li SR, Santosh M, Meng K, Dong GC, Wang YJ, Yin N, Ma GG, Yu HJ (2013) He-Ar isotope geochemistry of iron and gold deposits reveals heterogeneous lithospheric destruction in the North China Craton. J Asian Earth Sci 78:237–247

Sillitoe RH (2008) Major gold deposits and belts of the North and South American Cordillera—distribution, tectonomagmatic setting, and metallogenic considerations. Econ Geol 104:663–687

Song MC (2015) The main achievements and key theory and methods of deep-seated prospecting in the Jiaodong gold concentration area, Shandong Province. Geol Bull China 34:1758–1771 (in Chinese with English abstract)

Stefansson A, Seward TM (2004) Gold (I) complexing in aqueous sulphide solutions to 500 °C at 500 bar. Geochim Cosmochim Acta 20: 4121–4143

Storey CD, Jeffries TE, Smith M (2006) Common lead-corrected laser ablation ICP–MS U–Pb systematics and geochronology of titanite. Chem Geol 227:37–52

Stuart FM, Burnard PG, Taylor RP, Turner G (1995) Resolving mantle and crustalcontributions to ancient hydrothermal fluids: He-Ar isotopes in fluid inclusions from DaeHwa W-Mo mineralisation, South Korea. Geochim Cosmochim Acta 59:4663–4673

Su F, Xiao Y, He HY, Su BX, Wang Y, Zhu RX (2014) He and Ar isotope geochemistry of pyroxene megacrysts and mantle xenoliths in Cenozoic basalt from the Changle-Linqu area in western Shandong. Chin Sci Bull 59:396–411

Syverson DD, Ono S, Shanks WC, Seyfried JWE (2015) Multiple sulfur isotope fractionation and mass transfer processes during pyrite precipitation and recrystallization: an experimental study at 300 and 350°C. Geochim Cosmochim Acta 165:418–434

Tan J, Wei J, He H, Su F, Li Y, Fu L, Liu Y (2018) Noble gases in pyrites from the Guocheng-Liaoshang gold belt in the Jiaodong province: evidence for a mantle source of gold. Chem Geol 480:105–115

Tera F, Wasserburg GJ (1972) U-Th-Pb systematics in three Apollo 14 basalts and the problem of initial Pb in lunar rocks. Earth Planet Sci Lett 14:281–304

Wang YW, Zhu FS, Gong RT (2002) Tectonic isotope geochemistry—further study on sulphur isotope of Jiaodong Gold Concentration Area. Gold 23:1–16 (in Chinese with English abstract)

Wang J, Chang SC, Lu HB, Zhang HC (2016) Detrital zircon provenance of the Wangshi and Laiyang groups of the Jiaolai basin: evidence for Early Cretaceous uplift of the Sulu orogen, Eastern China. Int Geol Rev 58:719–736

Wang ZL, Yang LQ, Guo LN, Marsh E, Wang JP, Liu Y, Zhang C, Li RH, Zhang L, Zheng XL, Zhao RX (2015) Fluid immiscibility and gold deposition in the Xincheng deposit, Jiaodong Peninsula, China: a fluid inclusion study. Ore Geol Rev 65:701–717

Weatherley D, Henley RW (2013) Flash vaporisation during earthquakes evidenced by gold deposits. Nat Geosci 6:294–298

Wen BJ, Fan HR, Santosh M, Hu FF, Pirajno F, Yang KF (2015) Genesis of two different types of gold mineralization in the Linglong gold field, China: constrains from geology, fluid inclusions and stable isotope. Ore Geol Rev 65:643–658

Wen BJ, Fan HR, Hu FF, Liu X, Yang KF, Sun ZF, Sun ZF (2016) Fluid evolution and ore genesis of the giant Sanshandao gold deposit, Jiaodong gold province, China: constrains from geology, fluid inclusions and H-O-S-He-Ar isotopic compositions. J Geochem Explor 171:96–112

Williams-Jones AE, Bowell RJ, Migdisov AA (2009) Gold in solution. Elements 5:281–287

Xie SW, Wu YB, Zhang ZM, Qin YC, Liu XC, Wang H, Qin ZW, Liu Q, Yang SH (2012) U-Pb ages and trace elements of detrital zircons from Early Cretaceous sedimentary rocks in the Jiaolai Basin, north margin of the Sulu UHP terrain: provenances and tectonic implications. Lithos 154:346–360

Xue JL, Li SR, Sun WY, Zhang YQ, Zhang X, Liu CL (2013) Helium and argon isotopic composition in fluid inclusions and the source of ore-forming materials of Denggezhuang gold deposit in Jiaodong

peninsula. J Jilin Univ (Earth Sci Ed) 43:400–414 (in Chinese with English abstract)

Yan YT, Zhang N, Li SR, Li YS (2014) Mineral chemistry and isotope geochemistry of pyrite from the Heilangou gold deposit, Jiaodong Peninsula, Eastern China. Geosci Front 5:205–213

Yang JH, Chu MF, Liu W, Zhai MG (2003) Geochemistry and petrogenesis of Guojialing granodiorites from the northwestern Jiaodong Peninsula, eastern China. Acta Petrol Sin 19:692–700 (in Chinese with English abstract)

Yang JH, Chung SL, Zhai MG, Zhou XH (2004) Geochemical and Sr-Nd-Pb isotopic compositions of mafic dikes from the Jiaodong Peninsula, China: evidence for vein-plus-peridotite melting in the lithospheric mantle. Lithos 73:145–160

Yang KF, Fan HR, Santosh M, Hu FF, Wilde SA, Lan TG, Lu LN, Liu YS (2012) Reactivation of the Archean lower crust: implications for zircon geochronology, elemental and Sr-Nd-Hf isotopic geochemistry of late Mesozoic granitoids from northwestern Jiaodong Terrane, the North China Craton. Lithos 146:112–127

Yang KF, Jiang P, Fan HR, Zuo YB, Yang YH (2018) Tectonic transition from a compressional to extensional metallogenic environment at ~120 Ma revealed in the Hushan gold deposit. Jiaodong North China Craton J Asian Earth Sci 160:408–425

Yang LQ, Deng J, Goldfarb RJ, Zhang J, Gao BF, Wang ZL (2014) $^{40}Ar/^{39}Ar$ geochronological constraints on the formation of the Dayingezhuang gold deposit: new implications for timing and duration of hydrothermal activity in the Jiaodong gold province. China. Gondwana Res 25:1469–1483

Yang LQ, Deng J, Wang ZL, Guo LN, Li RH, Groves DI, Danyushevskiy L, Zhang C, Zheng XL, Zhao H (2016) Relationships between gold and pyrite at the Xincheng gold deposit, Jiaodong Peninsula, China: implications for gold source and deposition in a brittle epizonal environment. Econ Geol 111:105–126

Yang YH, Sun JF, Xie LW, Fan HR, Wu FY (2008) In situ Nd isotopic measurement of natural geological materials by LA-MC-ICPMS. Chin Sci Bull 53:1062–1070

Zhai MG, Santosh M (2013) Metallogeny of the North China Craton: link with secular changes in the evolving Earth. Gondwana Res 24:275–297

Zhang LC, Zhou XH, Ding SJ (2008) Mantle-derived fluids involved in large-scale gold mineralization, Jiaodong District, China: constraints provided by the He-Ar and H-O isotopic systems. Int Geol Rev 50: 472–482

Zhang Q, Xu RF, Xu F, Wang JH, Xiao BJ, Liu T, Yang XS (2006) Geological characteristics of gold deposits and ore-searching direction in Daliuhang area, Penglai city, Shandong province. Contri Geol Miner Resour Res 21:258–261 (in Chinese with English abstract)

Zhang ZR, Chen SZ (1999) Super large gold deposit exploration perspective in Jiaolai Basin of Jiaodong gold metallogenetic domain. Geochimica 28:203–212 (in Chinese with English abstract)

Zhang YQ, Li SR, Chen HY, Zhang XB, Zhou QF, Cui JC, Song YB, Guo J (2012) Trace element and He-Ar isotopic evidence of pyrite for source of ore-forming fluids in the Jinqingding gold deposit, eastern Shandong Province. Geol China 39:195–203 (in Chinese with English abstract)

Zhao Z, Zhao ZX, Xu JR (2012) Velocity structure heterogeneity and tectonic motion in and around the Tan-Lu fault of China. J Asian Earth Sci 57:6–14

Zhao R, Liu XF, Pan RG, Zhou M (2015) Element behaviours during alteration and mineralization: a case study of the Xinli (altered rock type) gold deposit, Jiaodong Peninsula. Acta Petrol Sin 31:3420–3440 (in Chinese with English abstract)

Zheng YF, Hoefs J (1993) Effect of mineral precipitation on the sulfur isotope composition of hydrothermal solutions. Chem Geol 105: 259–269

Zhou NW, Zhang Y (1997) An approach to genesis of visible gold in gold deposits in Penglai area. Shandong J Shenyang Instit Gold Technol 16:81–89 (in Chinese with English abstract)

Zhou TH, Lü GX (2000) Tectonics, granitoids and Mesozoic gold deposits in East Shandong China. Ore Geol Rev 16:71–90

Zhu RX, Chen L, Wu FY, Liu JL (2011) Timing, scale and mechanism of the destruction of the North China Craton. Sci China Earth Sci 54: 789–797

Zhu RX, Fan HR, Li JW, Meng QR, Li SR, Zeng QD (2015) Decratonic gold deposits. Sci China Earth Sci 58:1523–1537

Zou Y, Zhai MG, Santosh M, Zhou LG, Zhao L, Lu JS, Shan HX (2017) High-pressure pelitic granulites from the Jiao-Liao-Ji Belt, North China Craton: a complete P-T path and its tectonic implications. J Asian Earth Sci 134:103–121